Mechanistic Insights into the Electrochemical Reduction of CO₂ Catalyzed by Cyclopentadienone Iron Complexes

Supporting Information

Elisabeth Oberem,[a-c] Arend F. Roesel,[b] Alonso Rosas-Hernández,[c] Tobias Kull,[d,e] Steffen Fischer,[a] Anke Spannenberg,[c] Henrik Junge,[c] Matthias Beller,[c,*] Ralf Ludwig,[a-c,*] Michael Roemelt,[d,e,*] and Robert Francke[b,*]

[a]   LL&M Department, Rostock University, Albert-Einstein-Str. 25, 18059 Rostock, Germany; E-mail: ralf.ludwig@uni-rostock.de

[b]   Institute of Chemistry, Rostock University, Albert-Einstein-Str. 3a, 18059 Rostock, Germany; E-mail: robert.francke@uni-rostock.de

[c]   Leibniz Institute for Catalysis, Albert-Einstein-Str. 29a, 18059 Rostock, Germany; E-mail: matthias.beller@catalysis.de

[d]   Chair for Theoretical Chemistry, Ruhr-University Bochum, 44780 Bochum, Germany and

[e]   Max-Planck-Institut für Kohlenforschung, Kaiser-Wilhelm Platz 1, 45470 Mülheim an der Ruhr, Germany; E-mail: michael.roemelt@theochem.ruhr-uni-bochum.de

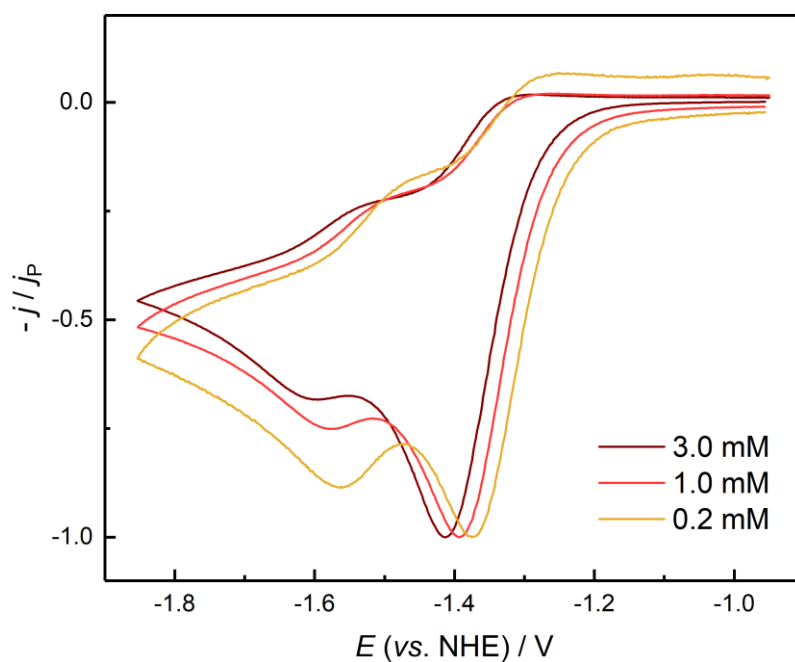## Content

1. Cyclic voltammetry

1.1 CV under Ar atmosphere

Figure S1. Cyclic voltammetry of **1b** under Ar atmosphere at various concentrations. Conditions: v = 250 mV s^{-1}, electrolyte = 0.1 M NBu$_4$ClO$_4$/CH$_3$CN, working electrode = glassy carbon disc.
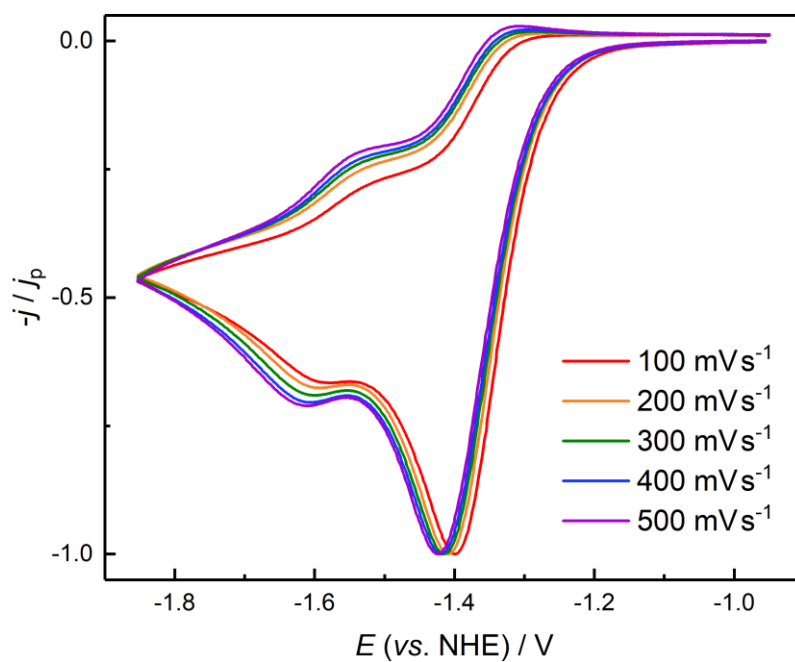

Figure S2. Cyclic voltammetry of **1b** under Ar atmosphere at various scan rates. Conditions: [**1b**] = 3 mM, electrolyte = 0.1 M NBu$_4$ClO$_4$/CH$_3$CN, working electrode = glassy carbon disc.

1.2 Digital simulations

The mechanisms depicted in Figure S3 were fitted to a CV recorded at $v = 250$ mV s^{-1}. In order to validate the obtained fitting parameters, they were applied to simulations of CVs recorded at different v in the range between 100 and 500 mV s^{-1} (see Figure S4). The standard deviations σ between the experimental and the simulated CVs were calculated from the current densities j_{exp} and j_{calc}, which are normalized with respect to the experimental peak current density $j_{p,exp}$ (see Figure S4). Equation (1)[1] was used for the calculation of σ, where n is the number of data points and p the number of fitted parameters.

$$\sigma = \sqrt{\frac{1}{n-p-1} \cdot \sum_n \left(\frac{j_{exp} - j_{calc}}{j_{P,exp}}\right)^2} \tag{1}$$

Mechanism A: E^1 $[(CO)_3Fe(L)] \xrightleftharpoons{+ e^-} [(CO)_3Fe(L)]^-$ $E_{P,1} = -1.4$ V

(see manuscript)   **1b**   **1b$^-$**

C^1 $[(CO)_3Fe(L)]^- \xrightarrow[- CO]{k_{c,1}} [(CO)_2Fe(L)]^-$

  1b$^-$ **4$^-$**

E^2 $[(CO)_2Fe(L)]^- \xrightleftharpoons{+ e^-} [(CO)_2Fe(L)]^{2-}$ $E_{P,2} = -1.5$ V

  4$^-$ **4^{2-}**

C^2 $[(CO)_2Fe(L)]^{2-} \xrightarrow[+ H^+]{k_{c,2}} [(CO)_2FeH(L)]^-$

  4^{2-}   **6$^-$**

parallel process:

C^3 $2\ [(CO)_2Fe(L)]^- \xrightarrow[+ H^+]{k_{c,3}} [(CO)_2Fe(L)]_2^{2-}$

  4$^-$ **3^{2-}**

Mechanism B: E^1 $[(CO)_3Fe(L)] \xrightleftharpoons{+ e^-} [(CO)_3Fe(L)]^-$ $E_{P,1} = -1.4$ V

"Father-and-son"   **1b**   **1b$^-$**

C^1 $[(CO)_3Fe(L)]^- \xrightarrow[- CO]{k_{c,1}} [(CO)_2Fe(L)]^-$

  1b$^-$ **4$^-$**

E^2 $[(CO)_2Fe(L)]^- \xrightleftharpoons{+ e^-} [(CO)_2Fe(L)]^{2-}$ $E_{P,2} = -1.5$ V

  4$^-$ **4^{2-}**

C^2 $[(CO)_2Fe(L)]^{2-} \xrightarrow[+ H^+]{k_{c,2}} [(CO)_2Fe(H)(L)]^-$

  4^{2-}   **5$^-$**

parallel process:

C^3 $[(CO)_2Fe(L)]^- + [(CO)_3Fe(L)] \xrightarrow{k_{c,3}} [(CO)_2Fe(L)]_2^- + CO$

  4$^-$ **1b**   **3$^-$**

E^3 $[(CO)_2Fe(L)]_2^- \xrightleftharpoons{+ e^-} [(CO)_2Fe(L)]_2^{2-}$ E_3
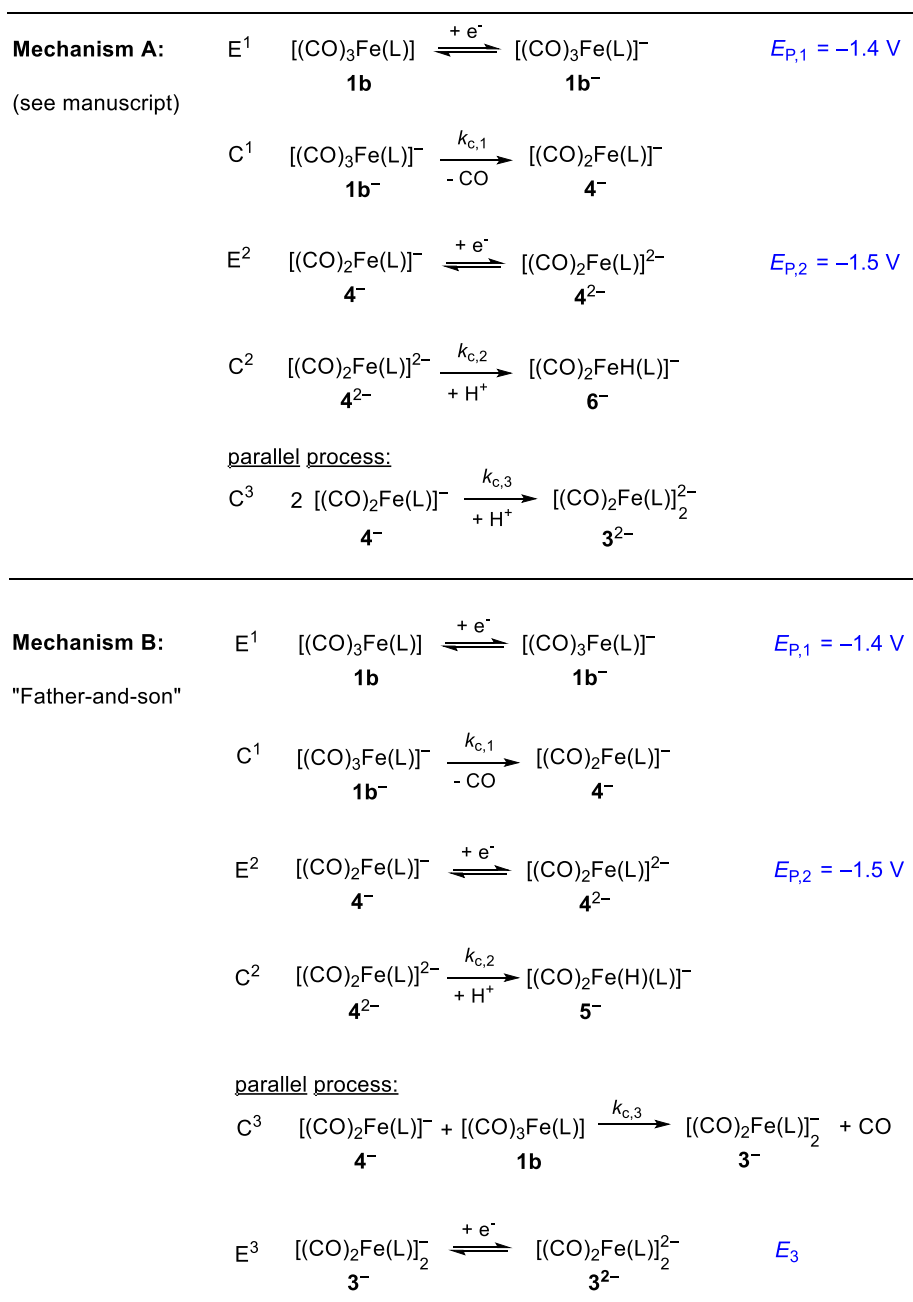
  3$^-$ **3^{2-}**

Figure S3: Mechanistic models for the simulations of the CVs of 3 mM **1b** recorded under Ar atmosphere.
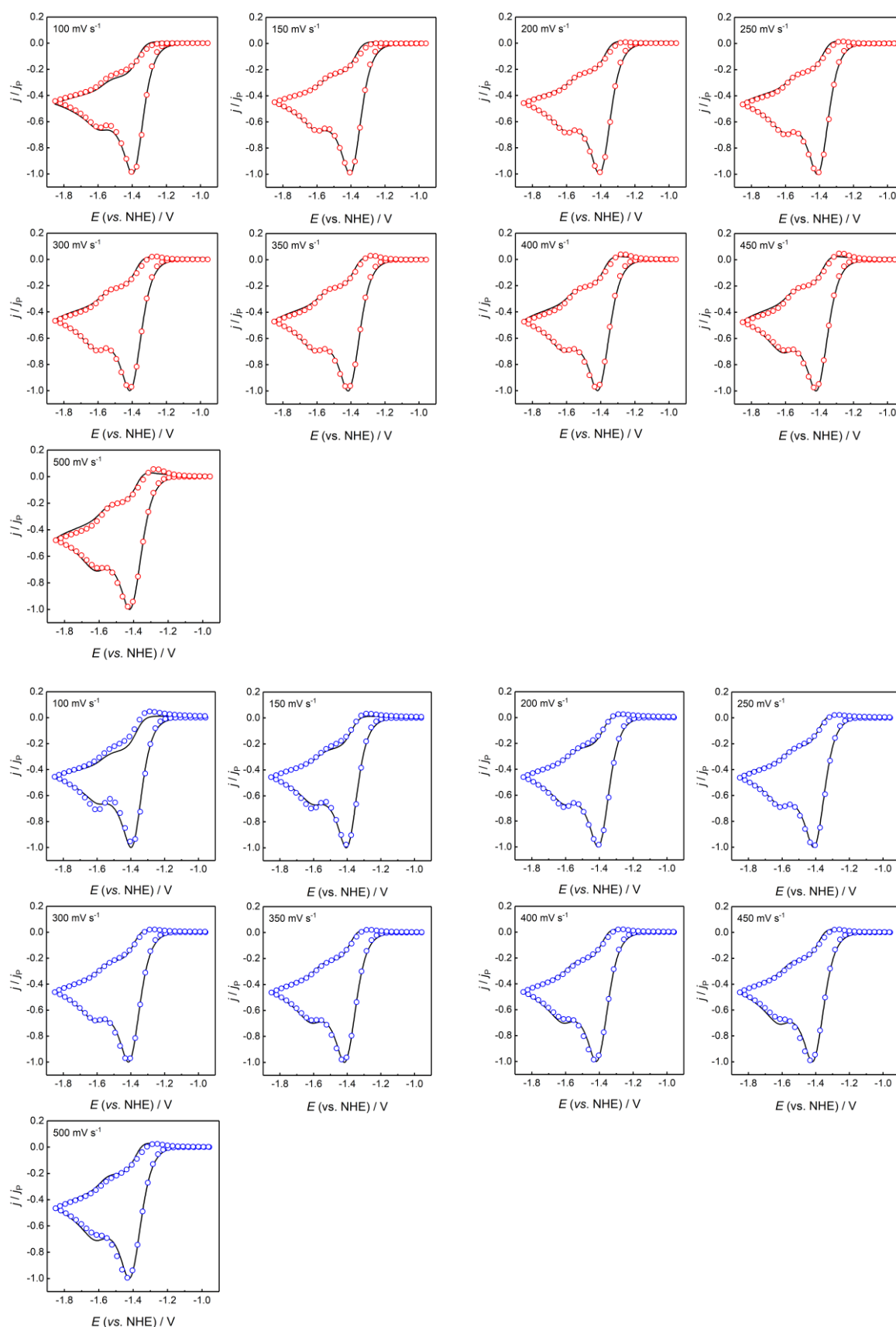
Figure S4. Cyclic voltammetry of **1b** under Ar atmosphere at various scan rates (black line: recorded CVs, circles: simulations). Experimental conditions: [**1b**] = 3 mM, electrolyte = 0.1 M NBu$_4$ClO$_4$/CH$_3$CN, working electrode = glassy carbon disc. The simulations were carried out based on the kinetic models shown in Figure S3 (red circles: mechanism A, blue circles: mechanism B).

Table S1. Fitting parameters for the digital simulations shown in Figure S4 and Figure 4 (see paper).

	Reaction Step	Parameter	Value
Mechanism A:	E^1	$E°$ (vs. NHE)	−1.3469 V
		α	0.48167
		k_s	$8.5886 \cdot 10^{-3}$ cm s^{-1}
		$D(\mathbf{1b}/\mathbf{1b^-})$	$2.6978 \cdot 10^{-5}$ cm^2 s^{-1}
	C^1	$k_{c,1}$	3.1388 s^{-1}
	E^2	$E°$ (vs. NHE)	−1.5721 V
		α	0.51422
		k_s	$5.11711 \cdot 10^{-3}$ cm s^{-1}
		$D(\mathbf{4^-}/\mathbf{4^{2-}})$	$1.2073 \cdot 10^{-6}$ cm^2 s^{-1}
	C^2	$k_{c,2}$ [a]	2.5912 s^{-1}
	C^3	$k_{c,3}$	330.96 L mol^{-1} s^{-1}
Mechanism B:	E^1	$E°$ (vs. NHE)	−1.3461 V
		α	0.46723
		k_s	$7.8683 \cdot 10^{-3}$ cm s^{-1}
		$D(\mathbf{1b}/\mathbf{1b^-})$	$2.9334 \cdot 10^{-5}$ cm^2 s^{-1}
	C^1	$k_{c,1}$	5.9123 s^{-1}
	E^2	$E°$ (vs. NHE)	−1.5786 V
		α	0.43691
		k_s	$1.6807 \cdot 10^{-3}$ cm s^{-1}
		$D(\mathbf{4^-}/\mathbf{4^{2-}})$	$2.819 \cdot 10^{-7}$ cm^2 s^{-1}
	C^2	$k_{c,2}$ [a]	8.741 s^{-1}
	C^3	$k_{c,3}$	181.16 L mol^{-1} s^{-1}
	E^3	$E°$ (vs. NHE)	−1.3398 V
		α	0.5
		k_s	0.1 cm s^{-1}
		$D(\mathbf{3^-}/\mathbf{3^{2-}})$	$1.0437 \cdot 10^{-6}$ cm^2 s^{-1}

[a]Since the proton source and its exact concentration in the protonation step C^2 is unknown (see discussion in the paper), pseudo-first order kinetics were assumed.

The influence of an additional protonation step leading to intermediate **5**, which occurred in parallel to the dimerization process was studied according to the following procedure: Mechanisms A and B (see Figure S3) were expanded by the additional protonation step C^4 shown in the following equation:

$$C^4 \quad [(CO)_2Fe(L)]^- \xrightarrow{\ k_{c,4}\ } [(CO)_2Fe(LH)]$$
$$\qquad\qquad \mathbf{4^-} \qquad\qquad\qquad\qquad \mathbf{5}$$
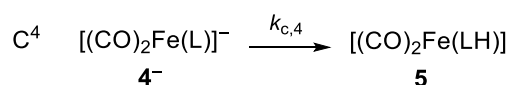
During the multiple fitting process, all parameters except the rate constant $k_{c,4}$ were held constant, whereby the latter one was optimized for different values of the rate constant of the dimerization $k_{c,3}$. For each received pair of rate constants the standard deviation between the corresponding fit and the experimental CVs at $v = 300$ mV s^{-1} was calculated according to equation (1). As shown in Figure S5 (top), σ reaches a minimum for each pair of $k_{c,4}$ and $k_{c,3}$ both for mechanism A and B, whereby this effect is more pronounced for mechanism B. These optimized pairs of rate constants (see Table S2) were applied together with the parameters from Table S1 to simulations at various scan rates. The standard deviations of these simulations show no considerable change compared to the simulations without taking C^4 into account (see Figure S5, bottom). Therefore, we can conclude that our kinetic model can also explain the formation of small quantities of **5**. We note that the major uncertainty in this consideration is the availability of protons and the change of the proton donor concentration in the course of the experiment (see discussion in the paper).
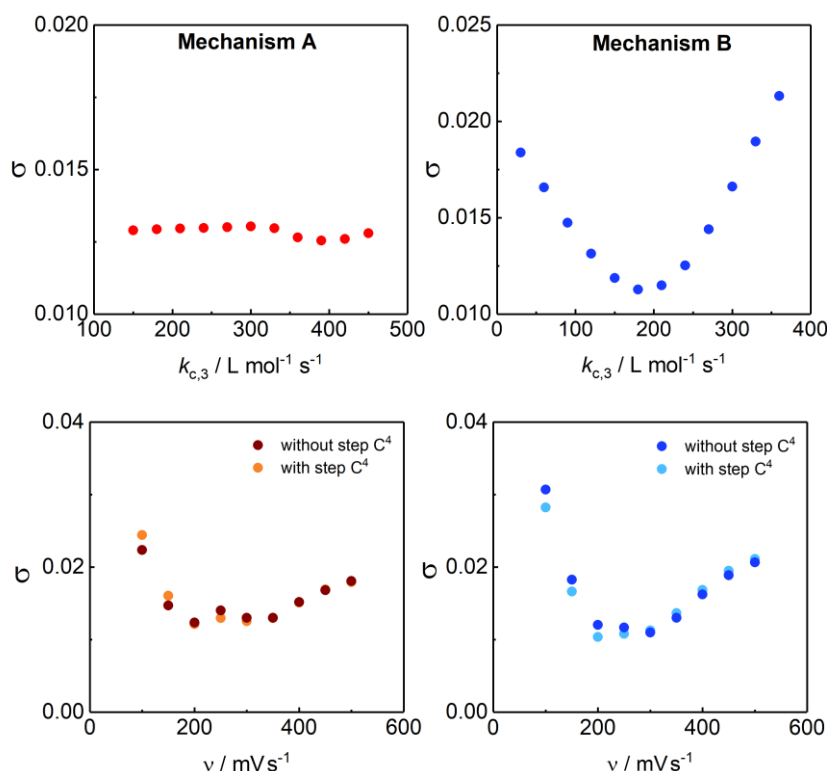
Figure S5. Inclusion of the additional protonation step C^4 in the digital simulations. Top: Standard deviation between experimental data ($v = 300$ mV s^{-1}) and fittings according to Mechanism A (left) and B (right) as a function of $k_{c,3}$ (see explanation in the text). Bottom: Standard deviation between simulations and experiments as a function of the scan rate (the parameters from Table S1 and Table S2 have been used for these simulations).

Table S2. Optimized rate constants for the mechanism shown in Figure S3 under inclusion of the additional chemical step C^4.

	Mechanism A	Mechanism B
With step C^4	$k_{c,3} = 390$ L mol^{-1} s^{-1} $k_{c,4}{}^a = 0.0021$ s^{-1}	$k_{c,3} = 180$ L mol^{-1} s^{-1} $k_{c,4}{}^a = 0.3657$ s^{-1}
Without step C^4 (compare Table S1)	$k_{c,3} = 330.96$ L mol^{-1} s^{-1}	$k_{c,3} = 181.16$ L mol^{-1} s^{-1}

[a]Since the proton source and its exact concentration in the protonation step C^4 is unknown (see discussion in the paper), pseudo-first order kinetics were assumed.

1.3 Studies under CO₂ atmosphere
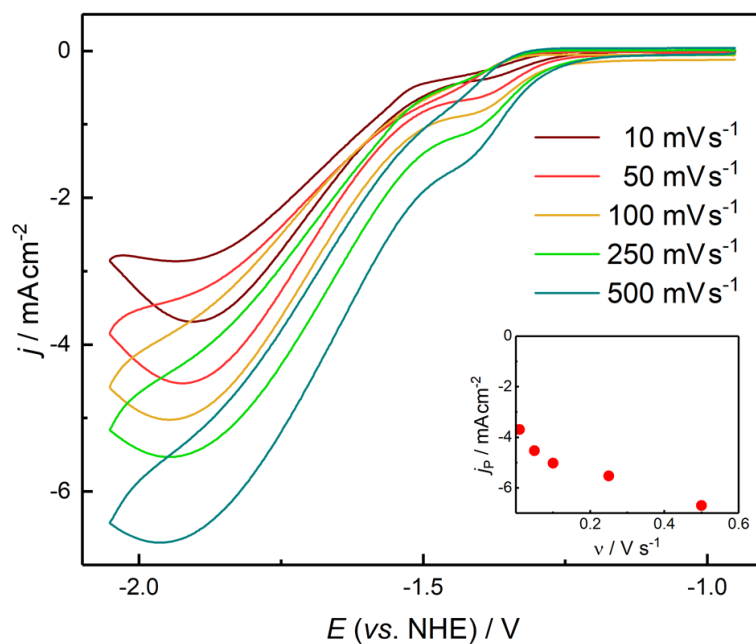
Figure S6. Cyclic voltammetry of **1b** under CO₂ atmosphere at various scan rates. Conditions: [**1**] = 1 mM, electrolyte = 0.1 M NBu₄ClO₄/CH₃CN, working electrode = glassy carbon disc.
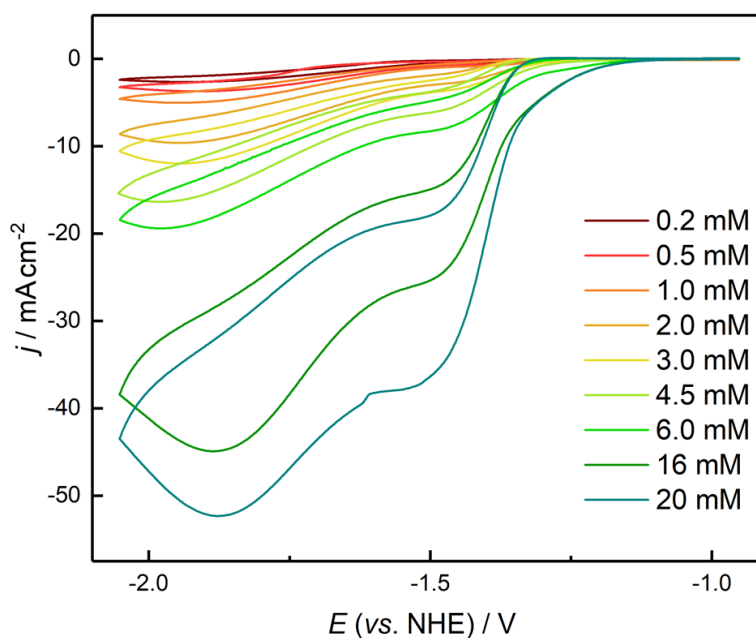
Figure S7. Cyclic voltammetry of **1b** under CO₂ atmosphere at various [**1b**]. Conditions: v = 100 mV s⁻¹, electrolyte = 0.1 M NBu₄ClO₄/CH₃CN, working electrode = glassy carbon disc. CVs with concentrations of 16 and 20 mmol L⁻¹ **1b** are recorded with *iR* drop correction.
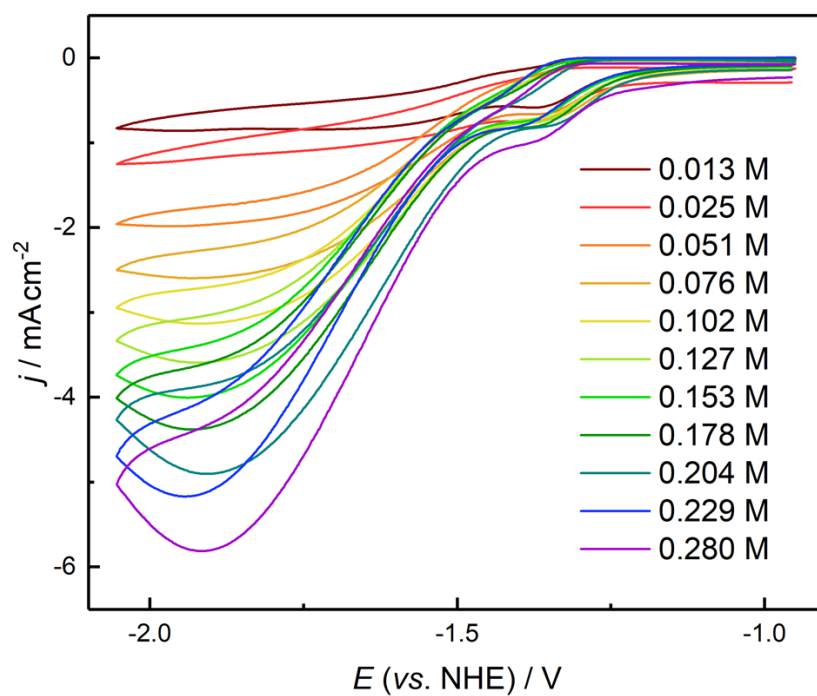
Figure S8. Cyclic voltammetry of 1 mM **1b** under CO_2 atmosphere at various [CO_2]. Conditions: $v = 100$ mV s^{-1}, electrolyte = 0.1 M NBu_4ClO_4/CH_3CN, working electrode = glassy carbon disc.
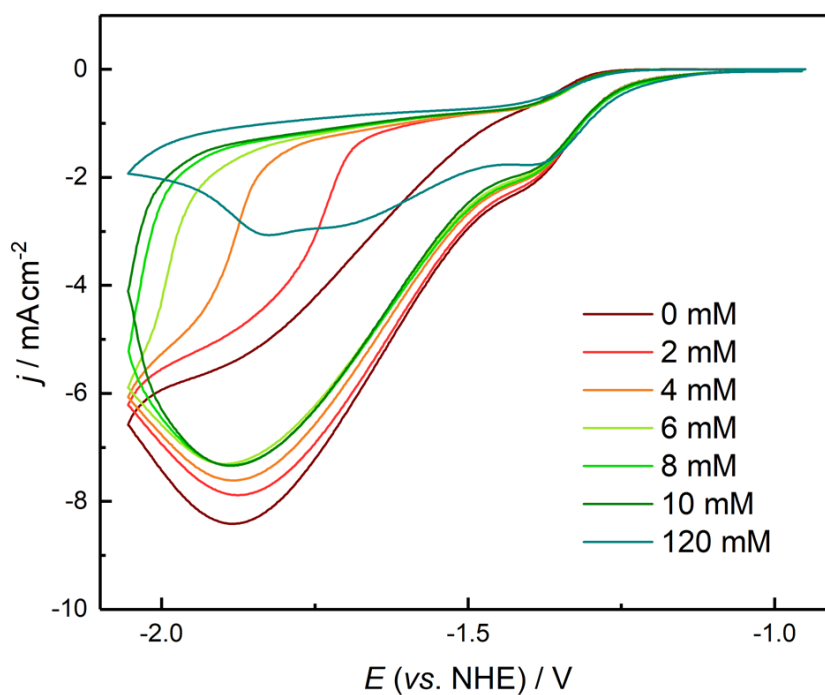
Figure S9. Cyclic voltammetry of 2 mM **1b** under CO_2 atmosphere after adding various amounts of H_2O. Conditions: $v = 100$ mV s^{-1}, electrolyte = 0.1 M NBu_4ClO_4/CH_3CN, working electrode = glassy carbon disc.
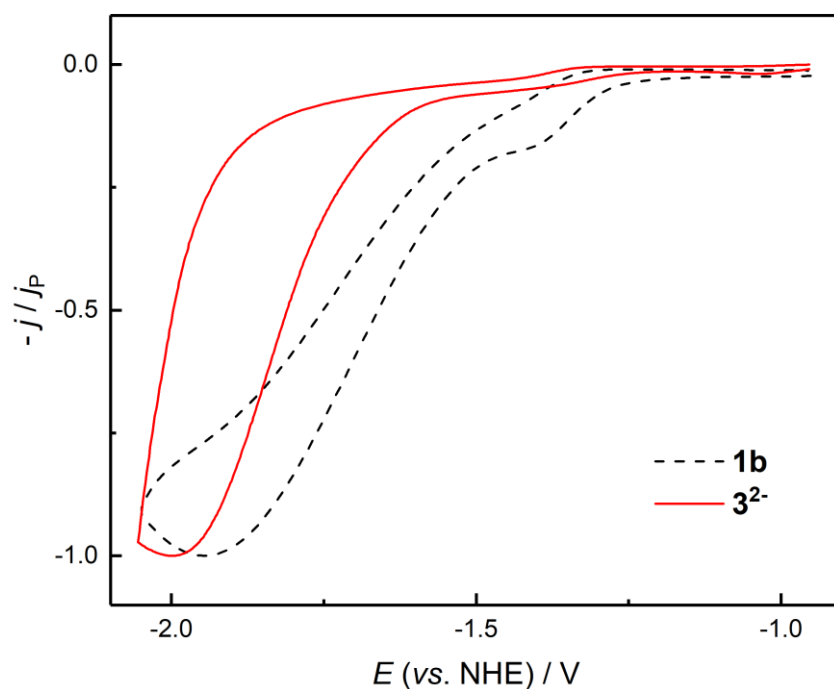
Figure S10. Cyclic voltammetry of a crystalline sample of 3^{2-} (dipotassium salt) under CO_2 atmosphere. Conditions: v = 100 mV s^{-1}, electrolyte = 0.1 M NBu_4ClO_4/CH_3CN, working electrode = glassy carbon disc. The CV of 1 mM **1b** is inserted for comparison. Due to the sensitivity of 3^{2-}, the mass (and the concentration) of the sample could not be exactly determined. For the sake of comparability, j was therefore normalized to the peak current density.
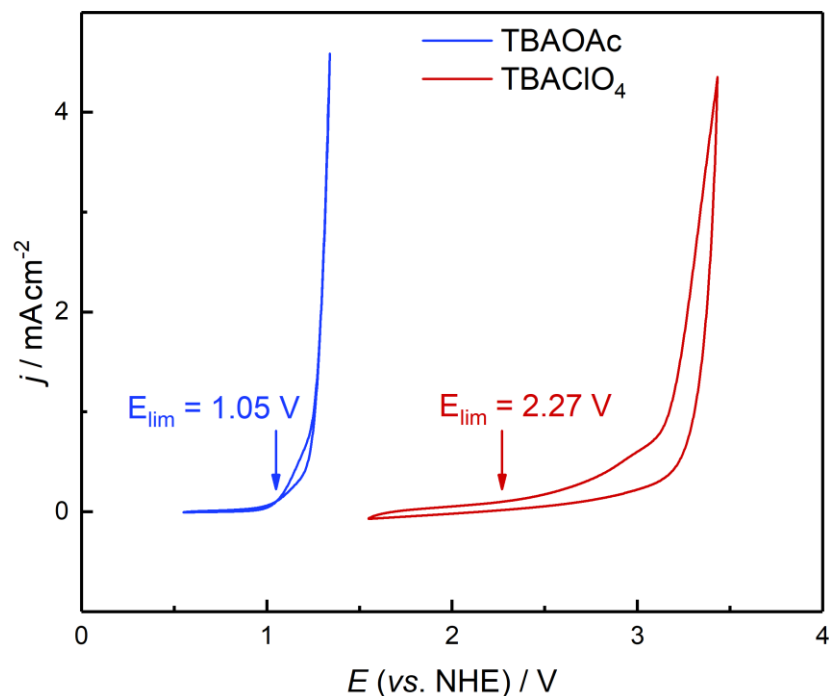
Figure S11. Cyclic voltammetry of 0.1 M TBAOAc (blue line) and TBAClO$_4$ (red line) in MeCN. Conditions: v = 100 mV s^{-1}, working electrode = glassy carbon disc. The limits of the electrochemical window E_{lim} are the potentials, where a limiting current density of 0.1 mA cm^{-2} is exceeded. The negative shift of E_{lim} for the acetate-based electrolyte with respect to the perchlorate-based solution demonstrates that acetate, and not the solvent acetonitrile, is oxidized first.

2. IR spectroelectrochemistry
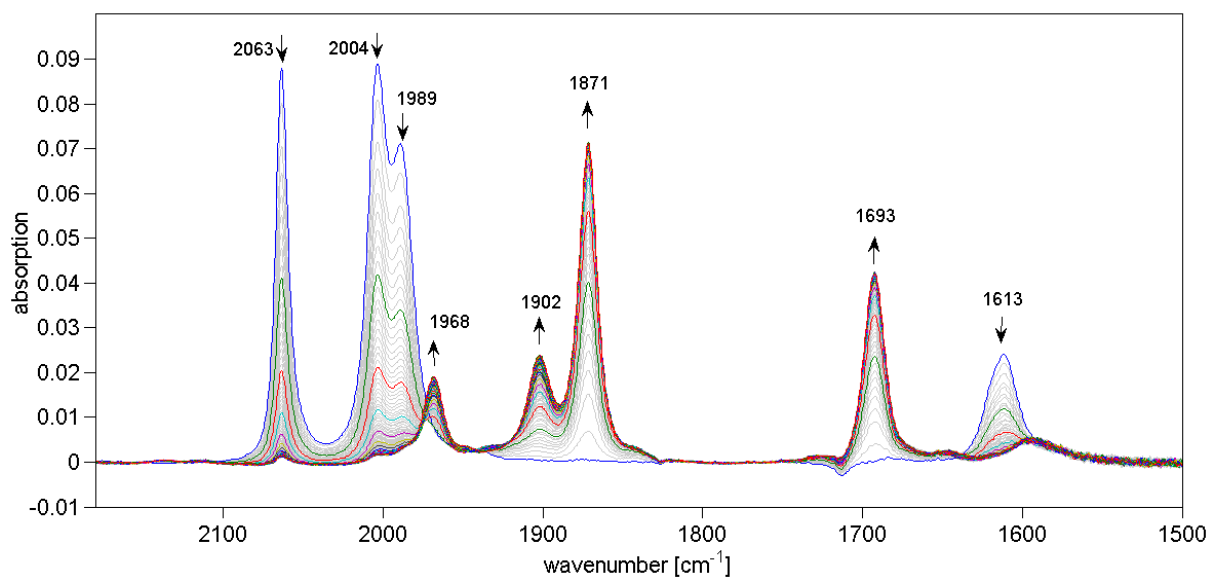
Figure S12. IR spectroelectrochemistry of 1 mM **1b** carried out under Ar at E = −1.9 V vs. Ag wire (duration: 300 s).
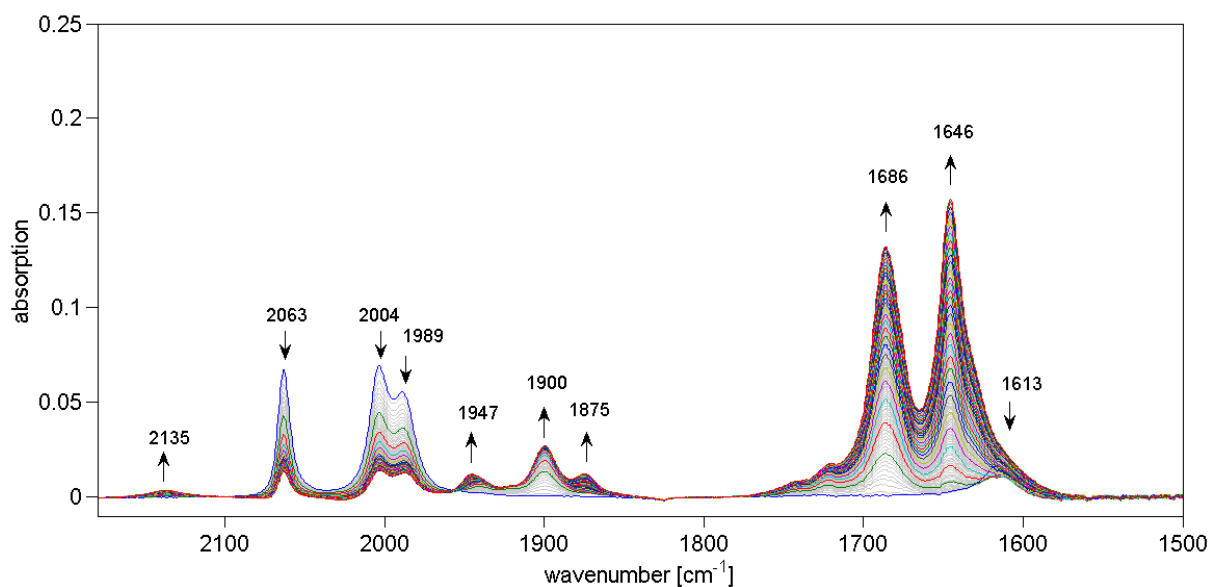
Figure S13. IR spectroelectrochemistry of 1 mM **1b** carried out under CO_2 at E = −2.1 V vs. Ag wire (duration: 300 s).

3. Chemical reduction of 1b

3.1 Identification of species 3^{2-}

As described in the experimental part of the paper, **1b** was reduced with two equivalents of KC_8 in THF in the presence of 18-crown-6, whereby green and red crystals were obtained. While the molecular structure determined via X-ray diffraction from the red crystals was determined to be **3^{2-}** (see Figure 3) no structural information could be obtained from the green crystals due to their polycrystalline nature. Portions of green and red crystals were separately dissolved in acetonitrile and subjected to IR spectroscopy (see Figure S14), which showed that both fractions contain dimer **3^{2-}**. Evidence that **3^{2-}** and not its monomer **4^-** represents the detected species in solution is provided by the match between the measured (1693 and 1872 cm^{-1}) and the calculated absorption bands (1697 and 1883 cm^{-1} for **3^{2-}**).
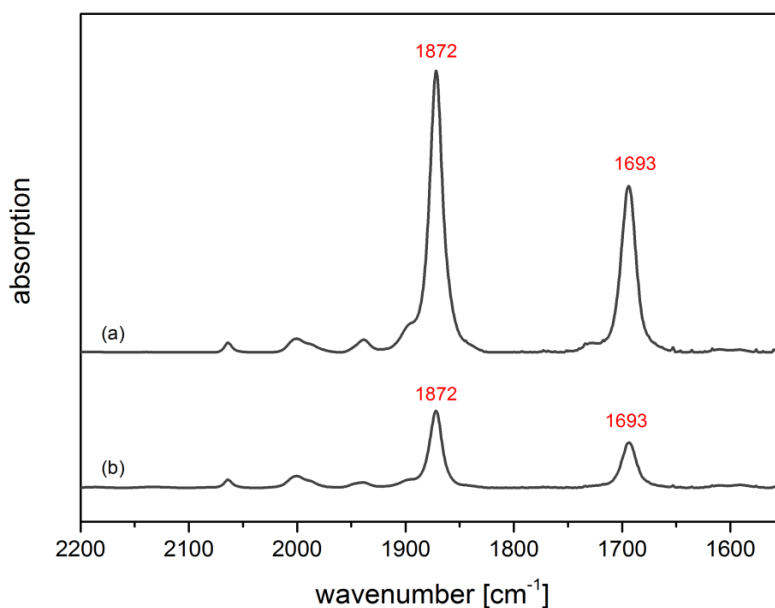
Figure S14. IR spectra recorded in CH_3CN of the red (a) and green (b) crystals obtained from reduction of **1b** with KC_8.

3.2 Identification of species 6^-
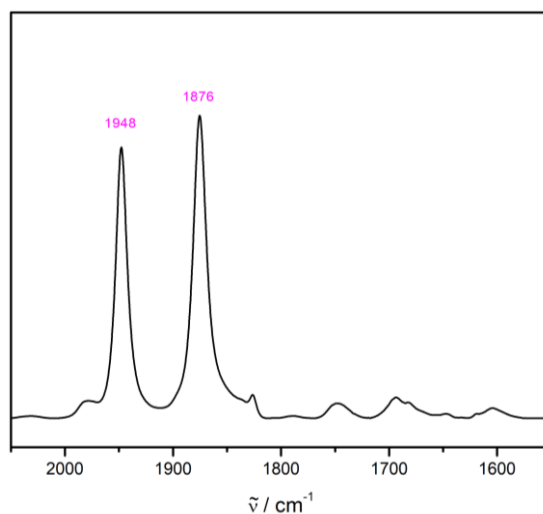
Figure S15. Solution IR spectrum of the intermediate resulting from the treatment of species **1b** with 5 equiv. KC_8.
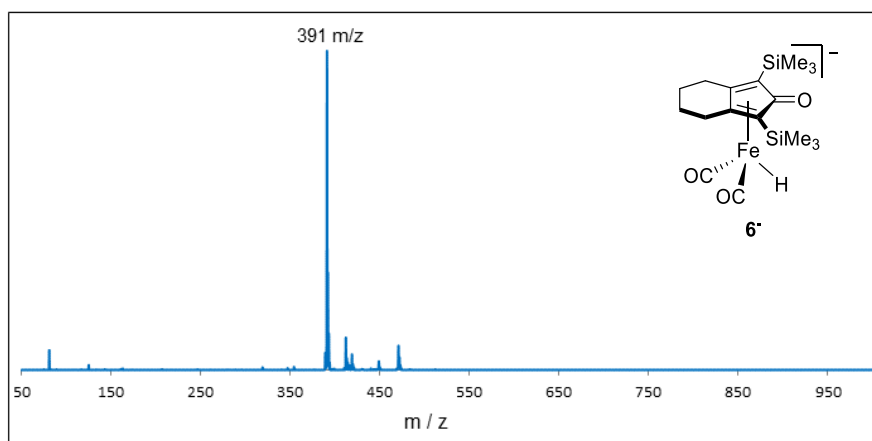
Figure S16. ESI-ITMS of the acetonitrile solution of intermediate **6⁻** resulting from the treatment of species **1b** with 5 equiv. KC$_8$. Spray temperature: 38 °C.
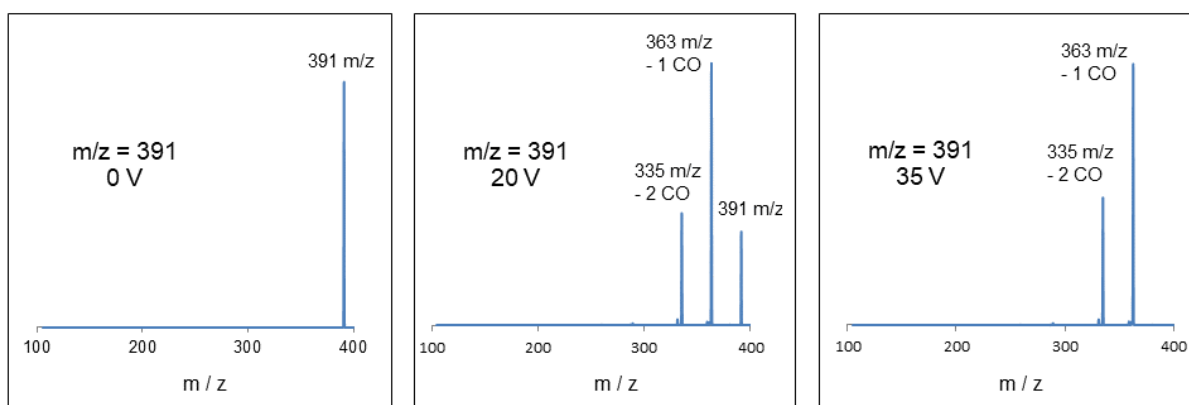
Figure S17. ESI-ITMS fragmentation experiments (CID) at m/z = 391 with U = 20 V (middle) and U = 35 V (right). Spray temperature: 38 °C.

3.3 The reactivity of 3^{2-} and 6^- toward CO_2

In order to test the reactivity of the observed intermediates toward CO_2, **1b** was first treated with two equiv. KC$_8$ in THF under Ar atmosphere and the reaction monitored with solution IR spectroscopy (see Figure S18). This treatment resulted in almost complete conversion of **1b** (spectrum a) to **3²⁻** and **6⁻** (spectrum b). This solution was saturated with CO_2, and another IR spectrum was recorded subsequently (spectrum c). While the bands associated with **6⁻** remained unchanged, the ones assigned to **3²⁻** disappeared. Concomitantly, the bands associated with **1b** reappeared, along with the bicarbonate band at 1684 cm⁻¹ and two new bands in CO stretching regime (1903 and 1938 cm⁻¹). We assign the band at 1903 cm⁻¹ to the same species appearing in the IR SEC experiment under CO_2 (see Figure 7, spectrum D).
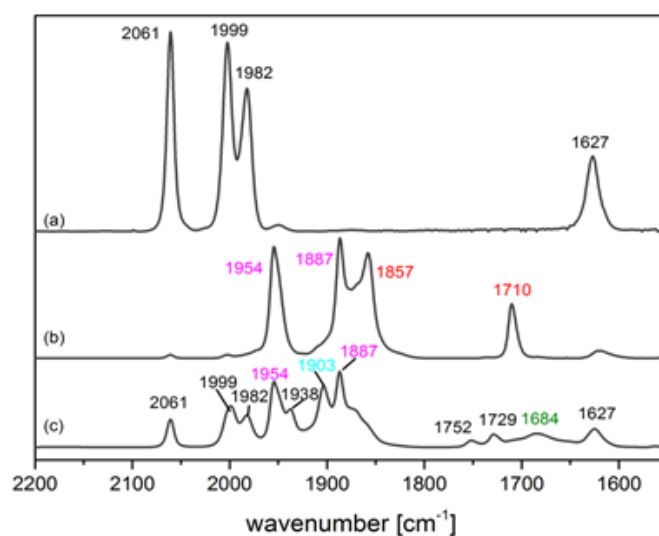
Figure S18. Monitoring of the chemical reduction of **1b** with two equiv. KC$_8$ in THF under Ar and subsequent conversion with CO$_2$. (a) Species **1b**. (b) Species **3^{2-}** and **6$^-$** resulting from the reduction of **1b** under Ar. (c) Reaction of **3^{2-}** and **6$^-$** with CO$_2$.

4. X-ray crystal structure analysis of [K(18-crown-6)]$_2$3

Crystal data: $C_{65.2}H_{114.4}Fe_2K_2O_{19.8}Si_4$, M = 1517.42, triclinic, space group $P\bar{1}$, a = 10.2236(2), b = 13.3523(3), c = 29.6370(7) Å, α = 101.1379(8), β = 91.0940(8), γ = 99.5957(8)°, V = 3908.46(15) Å^3, T = 150(2) K, Z = 2, 127537 reflections measured, 17046 independent reflections (R_{int} = 0.025), final R values ($I > 2\sigma(I)$): R_1 = 0.0305, wR_2 = 0.0791, final R values (all data): R_1 = 0.0366, wR_2 = 0.0837, 858 parameters.
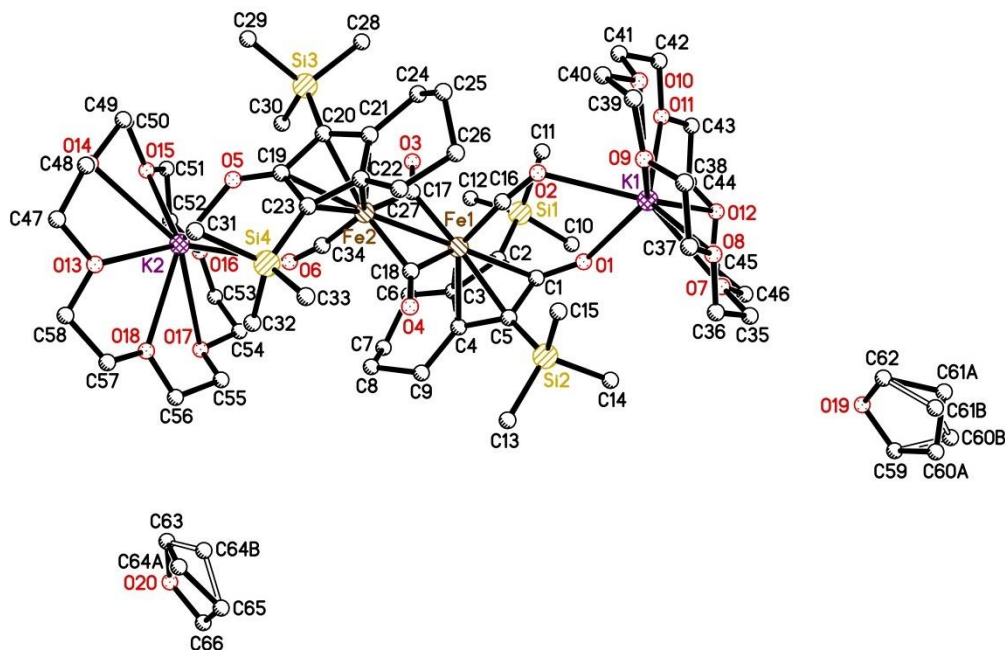
Ball and stick representation. Hydrogen atoms are omitted for clarity. The crystals contain co-crystallized disordered solvent molecules (disorder is depicted by open bonds). Selected bond lengths (Å) and angles (°): Fe1-C16 1.7421(15), Fe1-C17 1.9237(15), Fe1-C18 1.9268(15), Fe2-C17 1.9244(15), Fe2-C18 1.9294(15), Fe2-C34 1.7413(15), C1-O1 1.2709(17), C16-O2 1.1637(19), C17-O3 1.1856(19), C18-O4 1.1899(19), C19-O5 1.2680(17), C34-O6 1.1651(18), C1-C2 1.474(2), C2-C3 1.432(2), C3-C4 1.428(2), C4-C5 1.432(2), C1-C5 1.468(2), C19-C20 1.478(2), C20-C21 1.433(2), C21-C22 1.429(2), C22-C23 1.431(2), C19-C23 1.473(2), Fe1-Fe2 2.5779(3); C16-Fe1-C18 103.16(7), C16-Fe1-C17 93.29(7), C17-Fe1-C18 96.03(6), C34-Fe2-C18 103.19(6), C34-Fe2-C17 92.37(7), C17-Fe2-C18 95.92(6), Fe1-C17-Fe2 84.12(6), Fe1-C18-Fe2 83.91(6).

5.   Alternative mechanism

Pathway 1 including intermediate **7⁻** (see Scheme 7 in the paper) represents according to our IR SEC experiments and DFT calculations the most likely dimeric mechanism. However, an alternative route via **8⁻** (see Scheme S1) is also conceivable, since the latter species exhibits only a slightly inferior match between experimental and calculated IR spectrum.
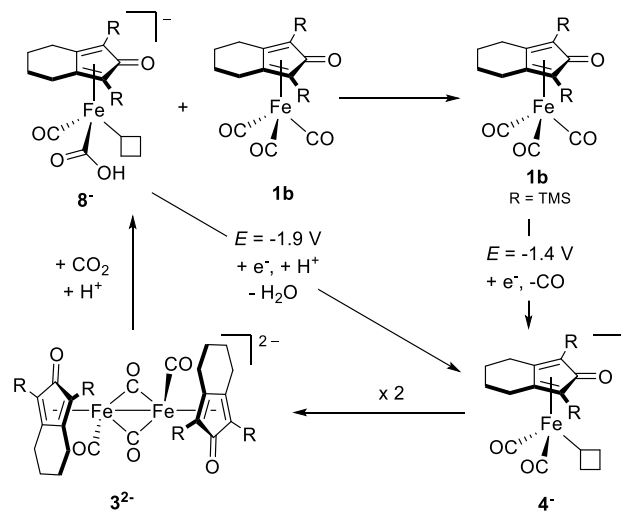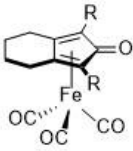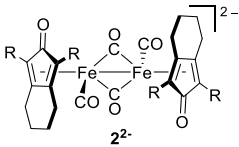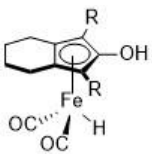
Scheme S1. Alternative to pathway 1 of the mechanism shown in Scheme 8.

6. Computational studies
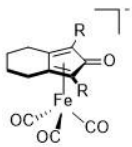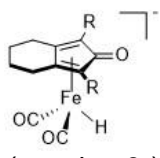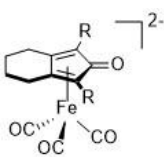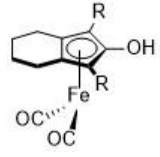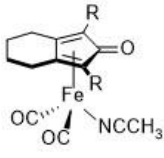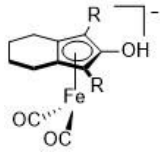
6.1 Computed IR frequencies
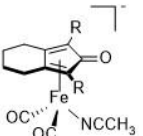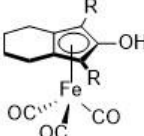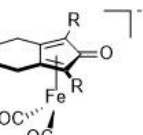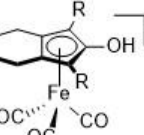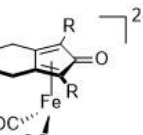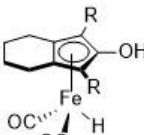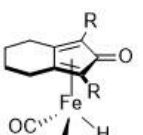
Table S3. Comparison between calculated and experimental IR frequencies of isolated and characterized compounds (R = TMS).

Entry	Compound	Experimental IR frequencies [cm^{-1}]	Calculated IR frequencies [cm^{-1}]
1		1613, 1989, 2004, 2063	1588, 1991, 2001, 2063
2		1693, 1872	(1501), 1698, 1883
3		1933, 1995[b]	(1907), 1929, 1996

[a] Values in parenthesis correspond to features that are not resolved in the experiment either because they are too weak or out of the energetic range of the experimental setup. [b] Reproduced from ref. [2].
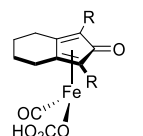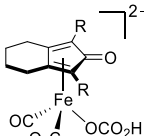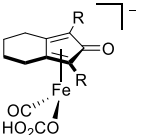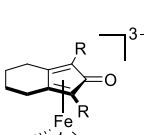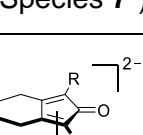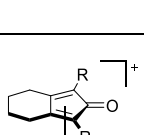
Table S4. Calculated IR frequencies[a] for a number of hypothetic intermediates (R = TMS).
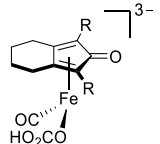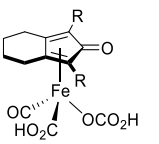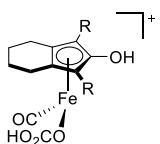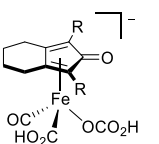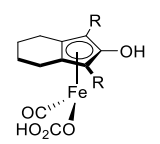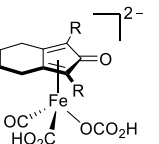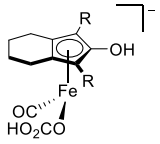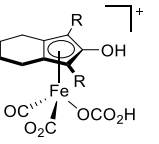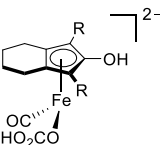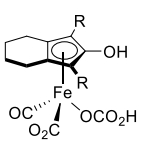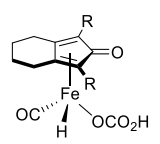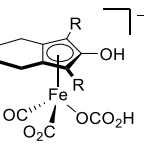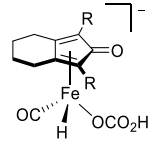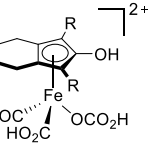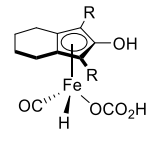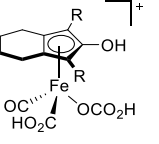
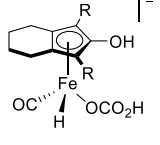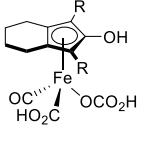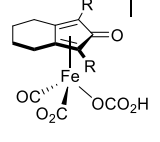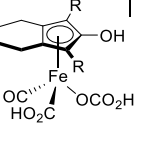| Entry	Compound	Calculated IR frequencies [cm^{-1}]	Entry	Compound	Calculated IR frequencies [cm^{-1}]
1		1550, 1856, 1868, 1953	8	(species **6$^-$**)	1506, 1868, 1873, 1949
2		1543, 1697, 1737, 1842	9	(species **5**)	1890, 1971
3		1569, 1947, 2002	10		1735, 1826

S17

Entry	Compound	Calculated IR frequencies [cm⁻¹]	Entry	Compound	Calculated IR frequencies [cm⁻¹]
4		1458, 1470, 1480, 1844, 1928	11		1473, 1932, 1935, 2015
5		1468, 1477, 1832, 1918	12		1492, 1786, 1808, 1910
6		1684, 1782	13		1907, 1929, 1996
7		1506, 1968, 2015			

[a]Frequencies were extracted from molecular Hessian calculations on the B3LYP-def2-TZVP(-f) level and scaled by a factor 0.9816 (see computational details).
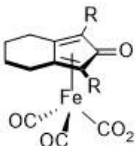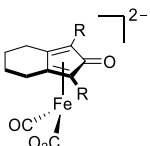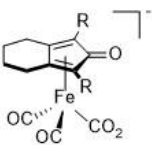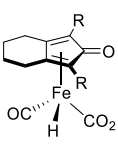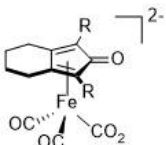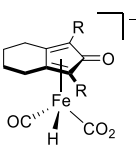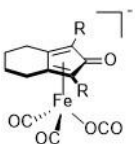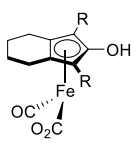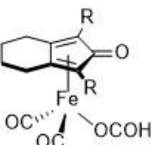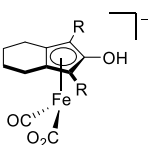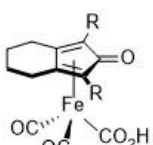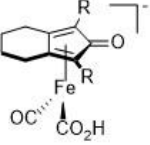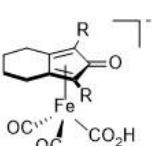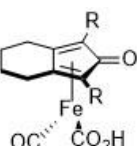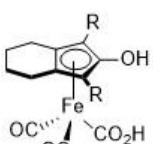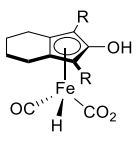
Table S5. Calculated IR frequencies[a] for a number of hypothetic bicarbonate adducts (R = TMS).
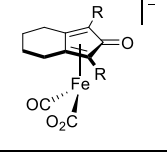
Entry	Compound	Calculated IR frequencies [cm⁻¹]	Entry	Compound	Calculated IR frequencies [cm⁻¹]
1		1462, 1575, 1669, 2045	14		1466, 1506, 1624, 1650
2	(Species **7⁻**)	1471, 1507, 1638, 1908	15		1485, 1649, 1819
3		1467, 1658, 1751	16		1467, 1527, 1713, 1726, 1774, 2119

#	Structure	Frequencies	#	Structure	Frequencies
4		1472, 1596, 1643	17		1469, 1515, 1632, 1646, 1704, 2037
5		1477, 1538, 2114	18		1469, 1539 1642, 1664, 1976
6		1467, 1647, 1977	29		1490, 1615, 1661, 1868
7		1467, 1669, 1827	20		1462, 1507, 1628, 2113
8		1466, 1634, 1668	21		1467, 1640, 1984, 2314
9		1477, 1609, 1647, 2005, 2024	22		1476, 1603, 1645, 1979
10		1464, 1518, 1646, 1839, 1944	23		1498, 1736, 1785, 2217
11		1467, 1656, 1915, 2016	24		1478, 1675, 1749, 2109
12		1478, 1633, 1777, 1890	25		1466, 1623, 1683, 2038
13		1466, 1518, 1650, 1913, 2294	26		1473, 1572, 1654, 1931

[a] Frequencies were extracted from molecular Hessian calculations on the B3LYP-def2-TZVP(-f) level and scaled by a factor 0.9816 (see computational details).

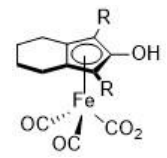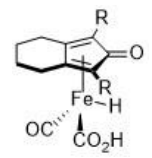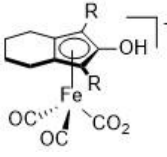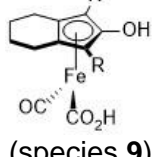Table S6. Calculated IR frequencies[a] for a number of hypothetic metallacarboxylates (R = TMS).

Entry	Compound	Calculated IR frequencies [cm^{-1}]	Entry	Compound	Calculated IR frequencies [cm^{-1}]
1		1563, 1954, 2012	12		1596, 1807
2		1541, 1725, 1920, 1970	13		1575, 1910, 1931, 2007
3		1484, 1510, 1848, 1924	14		1539, 1771, 1873, 1934
4		1470, 1480, 1827, 1916	15		1469, 1780, 1982
5		1603, 1613, 2049, 2083	16		1611, 1857
6		1575, 1636, 1998, 2035	17	(species **8⁻**)	1489, 1554, 1882
7		1531, 1628, 1902, 1967	18		1561, 1625, 2004
8		1970, 2025	19		1860, 1947, 1986

9		1897, 1977	20		1583, 1624, 1949, 1980
10		1547, 1900, 1919, 1982	21	 (species **9**)	1540, 1939, 1939
11		1499, 1696, 1932			

[a]Frequencies were extracted from molecular Hessian calculations on the B3LYP-def2-TZVP(-f) level and scaled by a factor 0.9816 (see computational details).

6.2 Relaxed surface scans
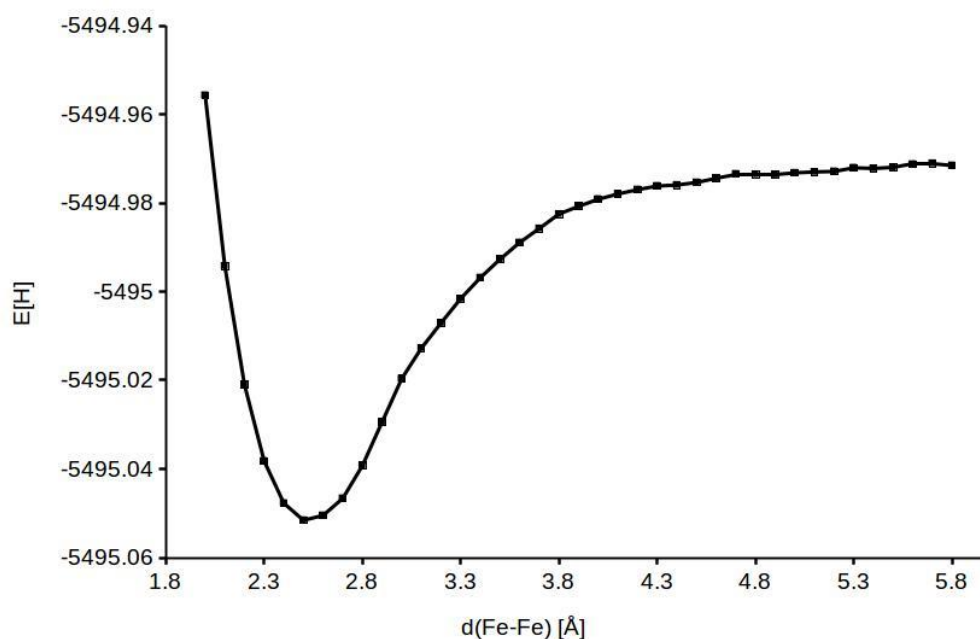
Dimerization of **4⁻** (formation of **3²⁻**):

Figure S19. Relaxed surface scan of the Fe-Fe bond distance of two molecules of **4⁻** on the BP86/def2-TZVP(-f) level of theory (see Computational Details section).

Protonation of **4⁻** (hypothetic formation of **6**):

Although geometry optimizations from different starting points with rather short Fe-carbonic acid distances were conducted, none lead to the desired Fe-hydride **6**. This finding together with the relaxed surface scan depicted in Figure S20 strongly indicates a reaction barrier of $\Delta G^{\ddagger}($**5/4⁻**$) > 0$ kcal mol⁻¹. However, despite immense efforts the true transition state between **4⁻** and **5** could not be located as the optimizations lead to transition states that connect different minima on the potential energy surface.
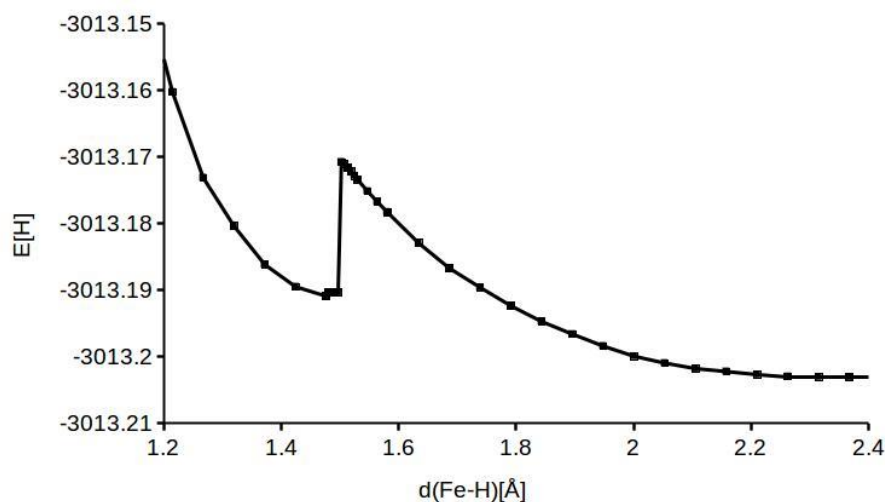

Figure S1. Relaxed surface scan of the Fe-H bond distance of **6** in the presence of carbonic acid on the B3LYP/def2-TZVP(-f) level of theory (see Computational Details section). The jump in energy around 1.5 Å originates from a sudden motion of the carbonic acid towards or away from the H, depending on the direction one follows the scan.

7. References

(1) Dowdy, S. M.; Wearden, S.; Chilko, D. M. *Statistics for Research*, 3rd Edition; John Wiley & Sons: Hoboken, N. J., 2005.

(2) Rosas-Hernández, A.; Junge, H.; Beller, M.; Roemelt, M.; Francke, R. *Catal. Sci. Technol.* **2017**, *7*, 459–465.